DETERMINATION OF THE OXYGEN PERMEABILITY OF METAL OXIDE THIN FILMS

A Thesis

Presented to the Faculty of the Graduate School

of Cornell University

In Partial Fulfillment of the Requirements for the Degree of

Master of Science

by

Rui Zeng

August 2018

ABSTRACT

Various metals such as Ta, Ti, W and their nitrides are often incorporated as thin films in integrated circuits as supportive and protective layers. For the films to be effective they must remain unoxidized. During IC manufacturing, thermal cycling can oxidize these thin films even if there is only a trace level of oxygen in the environment. If the metal or metal nitride is oxidized, it will no longer retain its functionality. Therefore, a diffusion barrier with low oxygen permeability is needed to protect these films during processing at elevated temperatures.

This work investigated the viability of Y_2O_3 and Al_2O_3 thin films as diffusion barrier by measuring the oxygen permeability between 300 °C and 500 °C. Diffusion barriers were deposited on a zirconium underlayer and were thermally oxidized in air. Optical reflectometry and ellipsometry were used to determine the thickness of the growing ZrO_2 layer; from this the oxygen diffusion flux and permeability were inferred.

ACKNOWLEDGMENTS

I would like to express my special thanks of gratitude to my advisor, R. B. Van Dover, and my committee member, Huili Xing, who give me this golden opportunity to do this wonderful study on oxygen permeability. Professor Van Dover and Professor Xing had supported me with tremendous amount of guidance that helped me stay on the right track along my academic research.

Second, I would like to thank Mats Larsson from Applied Materials Inc. who supported me through my industrial research with Applied Materials. I wouldn't have the opportunity to explore different types of thin film fabrication and characterization technologies without Mr. Larsson's support.

Last but not the least I would like to thank my parents and friends who helped me a lot in finalizing this project in the limited time frame.

TABLE OF CONTENTS

1. INTRODUCTION

Various metals such as Ta, Ti, W and their nitrides are often incorporated as thin films in integrated circuits as supportive and protective layers. For the films to be effective they must remain unoxidized. During IC manufacturing, thermal cycling can oxidize these thin films even if there is only a trace level of oxygen in the environment. If the metal or metal nitride is oxidized, it will no longer retain its functionality. Therefore, a diffusion barrier with low oxygen permeability is needed to protect these films during processing at elevated temperatures.

This work investigated the viability of Y_2O_3 and Al_2O_3 thin films as diffusion barrier by measuring the oxygen permeability between 300 °C and 500 °C. Diffusion barriers were deposited on a zirconium underlayer and were thermally oxidized in air. Optical reflectometry and ellipsometry were used to determine the thickness of the growing ZrO_2 layer; from this the oxygen diffusion flux and permeability were inferred.

2. BACKGROUND

- 2.1 Motivation

Various metal films that are widely used in IC manufacturing industry oxidize readily. For example, TiN, W_2N and Ta film are used as protective layers and supportive layers. TaN_x is often employed as an excellent barrier against Cu diffusion. ALD TaN has been reported to be an effective protective layer for Cu interconnects, for example by Kim et al. [1]. who investigated the diffusion barrier properties of an ultrathin PE-ALD TaN film. The excellent barrier properties were attributed to the nanocrystalline microstructure of the film. With increasing nitrogen content of the film, improved diffusion barrier properties have been achieved. However, TaN oxidizes readily when exposed to oxygen to form Ta_2O_5, which does not serve as a protective diffusion barrier for Cu. A research by Ibidunni et al. [2] had proved that TaN oxidize in air in a temperature range from 250 °C to 500 °C. Ibidunni also stated that TaN forms

passive Ta_2O_5 film when placed in air at room temperature. At higher temperature in air, oxygen diffuses through the passive Ta_2O_5 film and dissolves into the bulk. Therefor a protective layer that stops oxidation of TaN is needed at higher temperature. Various other metal layers such as Ti, W and their nitrides are widely used in nanofabrication as well and they all need to be similarly protected from oxidation if they are exposed to oxygen at high temperatures.

- 2.2 Diffusion in bulk crystal lattice

To understand atomic oxygen diffusion in thin films, the lattice diffusion mechanism must first be understood. In a bulk crystal lattice, diffusion is driven by the diffusant concentration gradient and is described by the impurity diffusion mechanisms. There are two impurity diffusion mechanisms: interstitial diffusion and vacancy (substitutional) diffusion. Impurities can occupy either an interstitial site or a substitutional site of a lattice (See Figure 1). Interstitial diffusion occurs when the concentration of the interstitial atoms is low so that only a small fraction of available site is occupied. Then each interstitial atom is surrounded by vacant interstitial sites. The interstitial atom can jump to another site as often as its thermal energy permits it to overcome the energy barrier of migration. This can be modeled by a random jump process. Vacancy diffusion happens when a substitutional atom exchanges its position with a vacancy. Normally the movement of the substitutional atoms is limited by occupancy of neighboring lattice sites by atoms, preventing motion. But when the adjacent site has a vacancy, the substitutional atom can jump to the vacancy site with a probability that depends on the probability that the substitutional atom can acquire sufficient vibrational energy. A schematic illustrating the two diffusion mechanisms is shown in Figure 2a and 2b. A combination of interstitial and substitutional diffusion can lead to a different diffusion mode, interstitialcy diffusion. Interstitialcy diffusion occurs when a substitutional atom jumps to an interstitial site and diffuses as an interstitial impurity. The mechanism of interstitialcy diffusion is shown in Figure 3c [3].

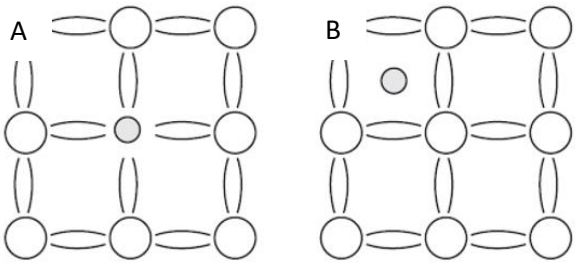

Figure 1. Impurities in lattice. A). Impurity occupies a substitutional site; B). Impurity occupies an interstitial site[3].

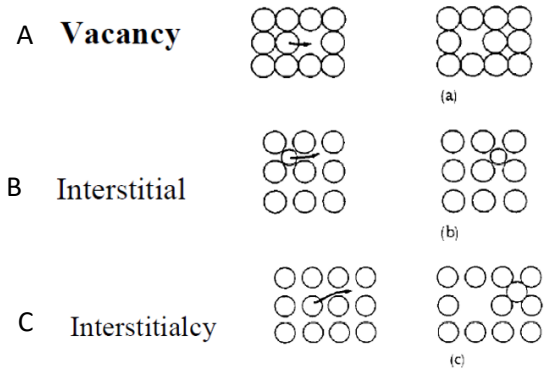

Figure 2. Impurity diffusion mechanisms in crystal lattice A). Vacancy diffusion; B). Interstitial diffusion; C). interstitialcy diffusion[3].

The diffusion kinetics for impurity diffusion in crystal lattice can be described by Fick's Law. Fick's first law relates the flux of atom diffusion to the concentration gradient across the diffusion media, and is given by [4]:

$$J = -D\frac{\partial C}{\partial x}$$

where *J* is the flux of diffusing atoms, *C* is the concentration of the diffusing atoms, *x* is the length measured normal to the *J*. and *D* is a constant associated with the diffusion process with dimension length^2/time. Fick's first law of diffusion implies that regions with large concentration gradient experience faster diffusion than regions with smaller concentration gradient. In a homogenous composition film, the film's oxygen concentration *C* and the diffusion coefficient *D* are constant. Therefore, oxygen diffusion in a homogenous composition film can be viewed as steady state diffusion.

Fick's first law of diffusion is only true in steady state where the diffusant concentration gradient is independent of position. In an inhomogeneous system, the concentration gradient can vary from point to point. Thus, Fick's second law of diffusion is introduced to describe this non-steady state

diffusion where the concentration function, *C(x)*, can be calculated as a function of time *t*. It is expressed as [4]:

$$\frac{\partial \mathrm{C}}{\partial t} = D\frac{\partial^2 \mathrm{C}}{\partial x^2}$$

In our application in which metal oxide thin films are used as an oxygen diffusion barrier, the oxygen concentration at each side of the barrier is unchanged once the oxidation of the Zr underlayer begins, and the oxygen concentration within the barrier is assumed independent of position, therefore the diffusion process can be characterized by Fick's first law of diffusion.

- 2.3 Enhanced oxygen diffusion in thin films

In addition to the oxygen self-diffusion in bulk and lattice, oxygen diffusion can be enhanced in thin film materials. The mechanism of thin film diffusion is more complicated as thin films contain more pathways for oxygen atoms transport. In polycrystalline thin films grain boundary diffusion can play an important role in atomic oxygen transport. An ^{18}O exchange study by Reddy [5] showed that oxygen diffusion along grain boundaries was enhanced compared to bulk (lattice) diffusion. Four different types of polycrystals were used in Reddy's study for exchanging in ^{18}O enriched gaseous environment and the ^{18}O profile was measured using a proton activation technique. To solve for oxygen grain boundary diffusivity, Reddy assumed that the penetration profile could be described by the Whipple-LeClaire approach [5], as $(C - C_\infty) vs. y^{6/5}$. Here, C is the surface concentration of ^{18}O, C_∞ is the native ^{18}O concentration and y is the penetration depth. Reddy's result showed that oxygen diffusion was enhanced along grain boundaries, so that the oxygen grain boundary diffusivity observed for polycrystalline alumina ($55\ {m^2}/{s}$) is much higher than the bulk oxygen lattice diffusivity for alumina ($1.5 * 10^{-2}\ {m^2}/{s}$) [5]. Reddy's finding was also supported by other polycrystalline ^{18}O exchange studies

by Oishi and Kingery [6], and Nakagawa et al. [5] that oxygen diffusion is greatly enhanced along grain boundaries.

- 2.4 Zirconium oxidation mechanism

Zirconium (Zr) oxidizes readily when exposed to oxygen; the amount of zirconia formed can be used as indicator for the amount of oxygen incorporated. To utilize this property of Zr as an indicator of oxygen fluence, the oxidation mechanism of metallic Zr must be understood. Jeurgens at al. [7] have shown that there are two modes of Zr oxidation: self-limiting oxidation at room temperature and the ongoing continuous oxidation at elevated temperature. The native zirconium oxide film is a non-stochiometric Zr oxide initially grown at the Zr metal interface. This layer of non-stochiometric ZrO_x is self-limiting and results in an oxide layer thinner than 2 nm. Jeurgens also showed that the native ZrO_x film contains a significant density of defects [7]. The film is observed to be O deficient near the metal-oxide interface. At elevated temperature, the second mode of Zr oxidation occurs, in which a layer of ZrO_2 forms on top of the non-stochiometric ZrO_x. Jeurgens found that at lower temperature (below 423 K), the newly-grown ZrO_2 film attains a limiting thickness; whereas above 423 K, the ZrO_2 film will grow continuously. XRD analysis showed that this newly grown Zr oxide is stochiometric crystalline ZrO_2 and the growth rate is limited by the diffusion of Zr cations toward the ZrO_2-O_2 interface. The overall Zr oxide growth curve and independent growth curves for the two oxidation stages are shown in Figure 3.

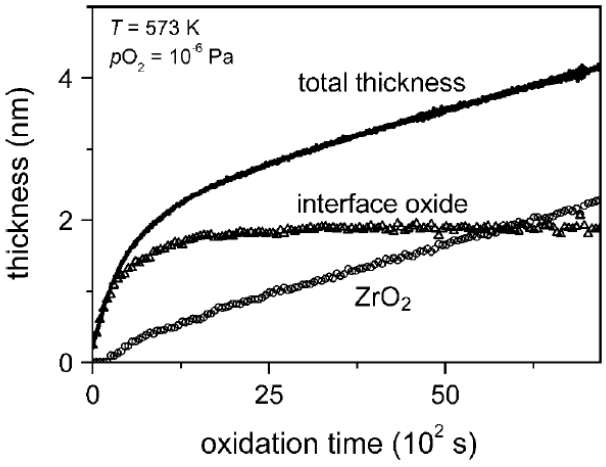

Figure 3. Individual growth curves and corresponding total growth curve for the non-stoichiometric interface-oxide (bottom) sublayer and the stoichiometric ZrO_2 surface (top) sublayer for the oxidation of the bare Zr substrate at 573 K and $pO_2 = 2x10^{-6}$ Pa [7]

This result agrees with another study that reveals the temperature dependence of Zr oxidation [8]. Figure 4 shows the total oxide formation curve for zirconium metal oxidized from 373 K to 573 K. Two stages of oxidation can be distinguished by the drastic slope change of the growth curve. It should be noted that the higher oxidation temperature corresponds to a larger limiting thickness in the first oxidation stage and a larger continuous growth rate in the second oxidation stage. Up to an oxide thickness of about 2-3 nm, relatively fast oxide growth is observed. Beyond the critical thickness of approximately 2 nm, the net electron transport via electron tunneling drops to zero and electron transport by thermionic emission becomes the rate-limiting factor (see below), so oxidation in the second stage is slower. The overall oxide film changes from amorphous, non-stochiometric Zr oxide at low temperature to crystalline stochiometric ZrO_2 at high temperature.

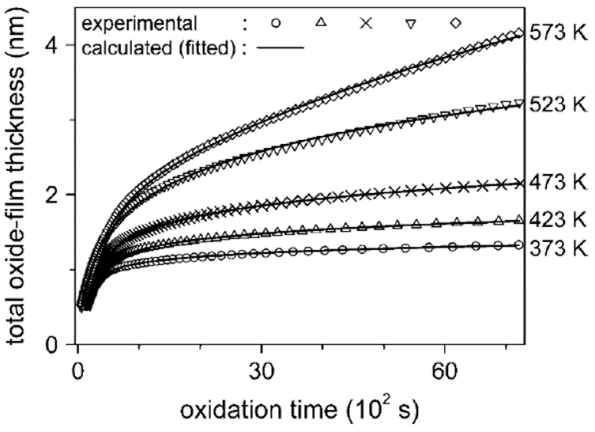

Figure 4. Total oxide growth curve as a function of time at various oxidation temperature. The experimental data were obtained by *in-situ* spectroscopic ellipsometry [7]

To determine the limiting factor for zirconium oxidation, the oxidation mechanism must be first understood by adopting the coupled current model. The formation of zirconium oxides is driven by the forward and reverse current within the zirconium metal due to electrostatic potential different between the Zr/oxide interface. In the initial stage of Zr oxidation, the oxide growth rate is limited by the Zr cation transport rate to the metal-oxide interface, where the nucleation of the Zr oxide starts. The driving force for electrons and Zr cation transport comes from surface charging and electron tunneling. Below the critical thickness (usually 2-3 nm, depending on temperature), the electron tunneling rate (providing the forward current) is significantly faster than the intrinsic electron diffusion rate (providing backward current), and the difference between these two currents create a homogeneous electric field at oxide

film surface and a kinetic potential V_k across the oxide film. The electric field is then equal to V_k/d, where d is the oxide film thickness. Zr cations are influenced by the electric field to move toward the oxide – gas interface. At the initial stage of Zr oxidation, a high electron tunneling rate is achieved due to the large electric field, providing large driving force for the Zr cation transport. Therefore, the initial stage of Zr oxidation is rapid, resulting in an amorphous and Zr-enriched native oxide film. After reaching the critical thickness, the effect of the electric field decreases and the electron tunneling rate essentially drops to zero. As a result, Zr cation transport can no longer be supported. However, the electron transportation via thermionic emission is independent of film thickness and is substantial at elevated temperatures. Therefore, in this stage the Zr cation transport is slow but with a constant rate . The oxidation reaction is then limited by Zr cations outward diffusion, resulting in crystalline fully-oxidized ZrO_2. Overall, the growth of Zr oxide is limited by Zr cation transport so every oxygen atom reaching the Zr surface will be converted to Zr oxide. Therefore, it is viable to utilize zirconium to indicate the quantity of oxygen presented to the surface of a Zr metal film.

- 2.5 Optical characterization methods

The oxygen diffusion flux through a thin film diffusion barrier can be estimated by finding the amount of oxygen incorporated in zirconium oxide, which can be calculated if the thickness of the ZrO_2 layer is known (Please see Chapter 3.2 for experimental setup details). Common film thickness measurement techniques include the stylus method, cross section TEM, XPS depth profiling, optical characterizations, etc [9]. Among other measurement techniques, optical characterization was chosen for this work because it is a non-destructive measurement, provides high accuracy, and is readily available. We use both a reflectometer and ellipsometor to provide accurate measurement of ZrO_2 film thickness.

- 2.5.1 Ellipsometry film measurement system

Ellipsometry film measurement systems are extensively utilized in industry to measure film thickness and other thin film properties such as refractive index (n) and absorption coefficient (k) as a function of wavelength by analyzing light refraction through the film [10]. The primary components for an ellipsometor system include: light source, polarization generator, sample, analyzer, and detector. The generally setup of an ellipsometor is illustrated in Figure5 [11]. The polarizer and analyzer are optical components that manipulate polarization of light. Incident light is linearly polarized after passing through the polarizer, on reflection by the film to be measured. The changes in polarization phase and amplitude of the light are analyzed and collected by the detector.

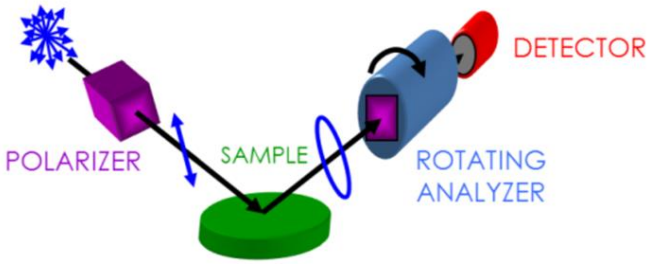

Figure 5. Typical setup of a ellipsometry film measurement

To understand the ellipsometry measurements, the wave nature of light must be understood. Light can be described as an electromagnetic wave traveling through space. For purposes of ellipsometry, it is adequate to discuss the electric field behavior in space and time, also known as polarization. The electric field of a wave is always orthogonal to the propagation direction. Therefore, a wave traveling along the z-direction can be divided by its electric field relative to the plane to the incident. The component of the electric field that is parallel to the plane is termed as p- and the component of the electric field that is normal to the plane is termed as s- [12]. Upon light reflection by the sample, the p- and s- polarized waves behave differently. Unpolarized light has completely random orientation and phase. For ellipsometry, however, we are interested in the electric field that follows a specific path, which is known as polarized light. There are three types of light polarizations: linear, circular and elliptical, each illustrated in Figure 6 [11]. When s- and p- components of the light are in-phase, the resulting light will

be linearly polarized (see Figure 6a). The relative amplitudes determine the resulting orientation. If the s- and p- components are 90° out-of-phase and equal in amplitude, the resulting light is circularly polarized (see Figure 6b). The most common polarization is when none of the above and is termed as "elliptical" (see Figure 6c). Elliptical polarization combines s- and p- components of arbitrary amplitude and phase.

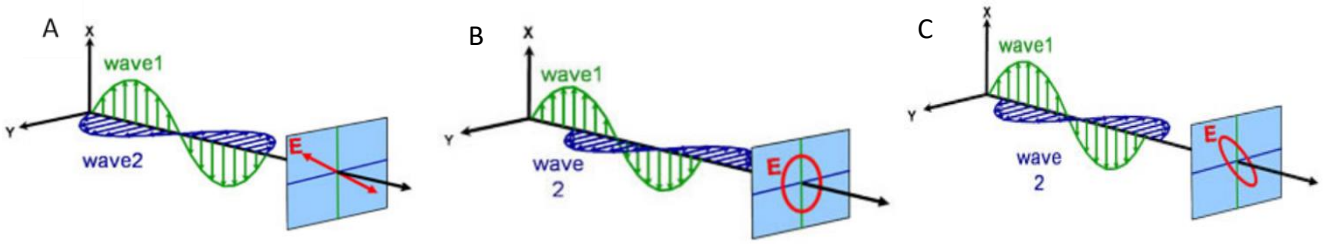

Figure 6. Three types of polarized light. A.) Linearly polarized; B.) Circularly polarized; C.) elliptically polarized [11]

Ellipsometry measures two values Δ and Ψ that represent the phase and amplitude changes of the p- and s-polarizations. Unpolarized incident light is sent through a polarizer which allows light of preferred electric field orientation to pass, transforming the incident light to linearly polarized light. Then the light is refleced from the sample surface, becomes elliptically polarized, and travels through a analyzer. The amount of light allowed to pass will depend on the analyzer orientation relative to the electric field of the light. The detector converts light to electronic signal Δ and Ψ to determine the polarization change caused by reflection on sample surface. Mathamatical model can be built to transform electrical signals Δ and ψ to film properties such as fim thickness.

Figure 7 [13] shows a flow chart of ellipsometor film analyzing procedure using a mathematical model of Δ and ψ. The model is used to calculate the predicted response from the Fresnel equations. If the film thickness and optical constants are not known, an estimate is given for the preliminary calculation. The calculated values are compared to experimental data of Δ and ψ. Any unknown material properties can be varied to improve the fitting between experimental and calculated. A good fitting is when the predicted Δ and ψ at every wavelength match with the experimental value and is considered as a good representation of the sample. Finding the best fitting is typically achieved through linear regression model.

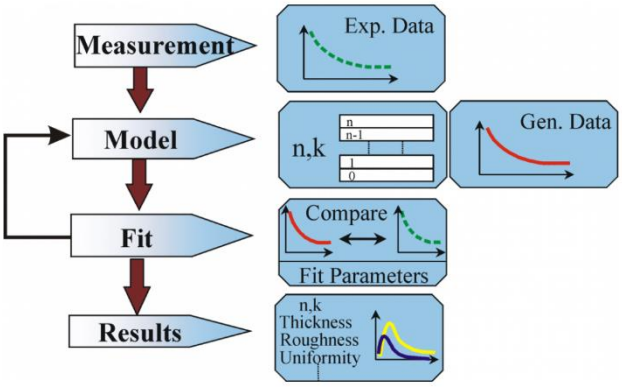

Figure 7. Flow chat of ellipsometry film analyzing procedure [13]

- 2.5.2 Reflectometry analyzing system

Reflectometry is another commonly used optical method and was extensively used in this study to measure the thickness of the ZrO_2 layer. Reflectometry analyzes light reflection by the sample to determine the optical properties such as refractive index, extinction coefficient and film thickness by measuring the reflected light intensity as a function of wavelength. This work used FilMetrics F50 tool as schematically shown in Figure 8. Here a source of incident light is set up to be incident perpendicular to the sample surface and reflected at a small angle back to a detector. The analyzer measures the relative intensity of the reflected light compared with the incident intensity. Film properties can be inferred by analyzing the wavelength-dependent relative intensity using an optical model.

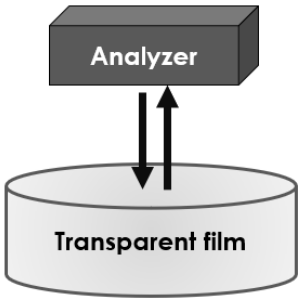

Figure 8. Set up of a FilMetrics film analyzing system

The refractive index (*n*) of a film is an intrinsic material property that describes light propagation through the medium. It is defined as:

$$n = \frac{c}{v}$$

where *c* is the speed of light in vacuum and *v* is the phase velocity of light in the medium. Light propagates slower in a material with a higher index than in a material with a lower index.

The extinction coefficient (*k*) is an intrinsic material property that measures how rapidly a material attenuates light through its thickness at a given wavelength λ. It is related to the absorption coefficient (α) of a material. The higher *k*, the stronger absorption [14]:

$$\alpha = \frac{4\pi k}{\lambda}$$

Light intensity loss due to absorption is characterized by:

$$I(x) = I_0 e^{-i\alpha x}$$

where *x* represents the relative location of light within the sample. Therefore, the extinction coefficient relates how quickly the light intensity decreases as it propagates in a material. Figure 9 [15] illustrates the light intensity loss due to absorption in a high *k* material.

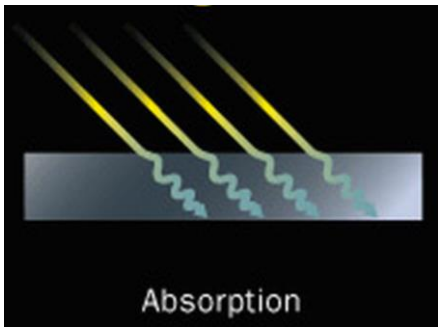

Figure 9. Light intensity loss due to absorption

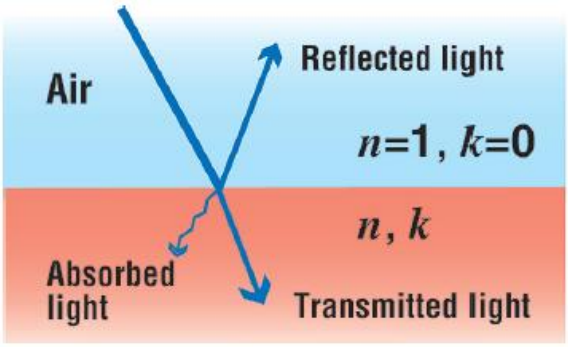

Figure 10. Light reflection at a single interface

Reflection occurs whenever light crosses the interface between different materials. The reflectance *R* is defined as the ratio of the intensity of reflected light to that of the incident light on a surface. It measures the effectiveness of a surface in reflecting light.

Figure 10 illustrates light reflection associate with crossing from one medium to another. Due to the difference in the refractive index of the two media, the speed of light will change. The change in phase velocity leads to a change in the light path, "bending the light" as shown in Figure 10. The reflectance of the reflected light is related to material properties *n* and *k* of the two mediums. It can be represented as [14]:

$$R = \frac{(n-1)^2 + k^2}{(n+1)^2 + k^2}$$

To see how *R* can be used to calculate optical constant, consider a simple case of light reflected from a single non-absorbing material (*k* = 0). Thus,

$$R = \frac{(n-1)^2}{(n+1)^2}$$

To obtain refractive index as a function of wavelength, one could plot the reflectance at each wavelength and derive *n* from the above equation.

Now consider a multilayered system, where a thin film is on top of another material, as shown in Figure 11 [14]. In this case, both the top and bottom of the thin film reflect light. The total amount of light is the superposition of these two individual reflections. Because of the wavelike nature of light, the superposition of the two reflected lights may be either constructive or destructive, depending upon

their phase relationship. The phase relationship is determined by the optical path lengths that light travels through the films, which is determined by the optical constants, film thickness and wavelength of the incident light. When the light path is equal to a multiple of the light wavelength, the two reflections are in-plane and add constructively. In the case of reflectometer system, light incidents perpendicular to film surface so that the reflected and refracted angle are both 0 degree. Constructive superposition occurs at $2nd = i\lambda$, where λ is the wavelength of the incident light; d is the film thickness and i is an integer. When the two reflections are out of phase, the two reflected lights add destructively. This happens when $2nd = (i + \frac{1}{2})\lambda$. These reflections may be added to a single equation:

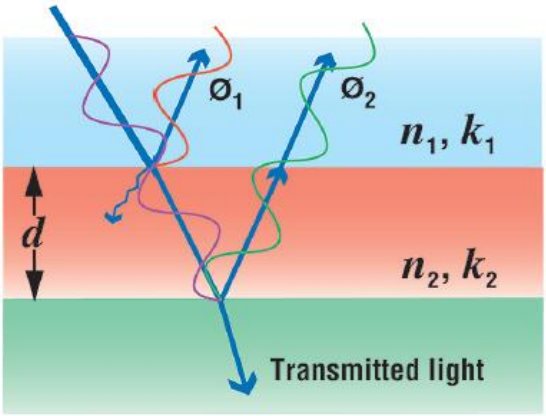

Figure 11. Multi-reflection system [14]

$$R = A + B\cos(\frac{4\pi}{\lambda})_{nd}$$

The reflectance spectrum is a plot of reflectance *R* as a function of wavelength. In reflectometry measurement, the film properties are determined by calculating spectral reflectance based on trial values of film thickness and the *n* and *k* model parameters, and then adjusting these values until the calculated reflectance spectra matches the measured one. Therefore, the thickness of the film can be estimated by building a mathatical model of the film stack with known *n* and *k*. In our case, the thickness of the ZrO_2 layer can be estimated using such method and the amout of oxygen passing though the barrier can be calculated by estimating the amount of oxygen in the ZrO_2 film.

- 2.6 Determine the oxygen permeabilty of the barrier film

The permeability constant, *P*, is a measure of the ability of a porous material to allow a substance to pass through it. For thin film materials, which higher defect density is expected than bulk materials,

diffusion through grain boundaries and defects can have a large impact on the permeability constant. If we assume steady state diffusion and constant diffusion coefficient, the relationship between permeability (*P*), solubility (*S*) and diffusion coefficient (*D*) simplifies to [16]

$$P = D * S \tag{1}$$

With reference to the prior introducton to diffusion (Chapter 1.2), solublity will be disscussed in the following section.

- 2.6.1 Gas solibility in solid

The gas solubility, *S*, in the thin film, is the maximum amount of gas that can be dissolved at a specified temperature. The extent of the solubility of a substance in a specific solvent is measured as the saturation concentration, where adding more solute does not increase the concentration of the solution and will just escape from the solid [16]. For metal oxide thin film, at steady-state, the solubility of oxygen is approximated to be the oxygen concentration in the compound. The unit of solubility is mol/cm^3 and can be estimated by finding the molar concentration of the solvent in the barrier film. The oxygen solubility of Al_2O_3 is estimated to be 0.116 mole/ cm^3 and 0.0666 mole/ cm^3 for Y_2O_3.

- 2.6.2 Converting diffusion flux to permeability

As mentioned in Chapter 1.2, atomic diffusion flux, *J*, is the rate of mass transfer per unit area of section. In our diffusion barrier system, the oxygen concentrations at each side of the barrier film are different, C_1 and C_2 respectively, and everywhere uniform within the diffusion barrier so the diffusion coefficient is constant. The rate of diffusion per unit area is calculated by

$$J = -D\frac{\partial C}{\partial x} = \frac{D(C_1 - C_2)}{t} \tag{2}$$

Here t is the thickness of the barrier. C is the oxygen concentration at each side of the barrier, with C_1 is the oxygen concentration in air and C_2 is the oxygen concentration in Zr film and is approximated to be zero. The rate of diffusive transfer can be rewritten as

$$J = \frac{D * C_1}{t} \tag{3}$$

Plug equation (3) back to (1), we can obtain the relationship between permeability and diffusion flux

$$P = \frac{J * t * S}{C_1} \tag{4}$$

3. EXPERIMENTAL APPROACH

- 3.1 Materials selection

The goal of these experiments is to measure the oxygen permeability of metal oxide thin films, as a function of temperature, oxidation time and film thickness, and thereby to evaluate the performance of each film as an oxygen diffusion barrier. Ideal barrier materials for this study should be expected to have low oxygen permeability, excellent mechanical properties and be robust with respect to thermal cycling. We chose two oxides with different crystal structure. The literature [17] suggests that the dense hexagonal close pack corundum and bixbyite crystal structures should exhibit lower permeability than more open fluorite lattice. Therefore, oxides with corundum and bixbyite structure were chosen and tested in this study.

Alumina, Al_2O_3 has been reported to be a good diffusion barrier against oxygen at low temperatures. The diffusion coefficient in amorphous Al_2O_3 was reported to be $2.5x10^{-22}$ m^2s^{-1} [18]. Alumina can be prepared with the bixbyite structure but the most common form is corundum with

oxygen atoms hexagonally close packed [5]. Although it is well established that Al_2O_3 is able to prevent oxygen diffusion at low temperature, its effectiveness at elevated temperature is not well established. Oishi and Kingery [6] reported an exponential increase in polycrystalline alumina diffusion coefficient with increasing temperature up to 1700°C. The diffusion coefficient at 1700°C was reported to be ~10^{-16} m^2s^{-1} and its effectiveness as oxygen diffusion barrier is highly questionable. Furthermore, alumina has high thermal expansion coefficient ($8.1x10^{-6}$ K^{-1} [19]) compared to Si ($3\text{-}5x10^{-6}K^{-1}$ [20]). The thermal stress created by thermal cycling might affect its effectiveness as an oxygen diffusion barrier if it is mechanically constrained by a Si substrate.

Other materials, such as those with the bixbyite structure, are expected to work well against oxygen diffusion. Y_2O_3 is a cubic bixbyite that is robust against plasma erosion damage. Kitamura et al. had investigated the anti-plasma erosion resistance of plasma sprayed Y_2O_3 and compared that with the traditional techniques such as alumite film and bulk ceramics [21]. Kitamura et al. concluded that Y_2O_3 coating has higher anti-plasma erosion resistance than alumina coating and traditional alumite film. Y_2O_3 single crystal was reported to have an oxygen diffusion coefficient of 10^{-15} m^2s^{-1} at 1000°C. Its effectiveness as oxygen diffusion barrier is not well established.

- 3.2 Testing system

To measure the oxygen permeability of the diffusion barrier, Oxygen diffusion flux must be quantified by finding the amount of oxygen passed through the diffusion barrier per unit area and time. This could be done by applying an oxygen indicator that counts numerically the moles of oxygen molecules passed through the diffusion barrier in a given time. As previously discussed in chapter 1.4, Zr could be the choice of oxygen indicator. The mechanism of Zr oxidation is limited by Zr cations transporting to Zr surface. This ensures that every oxygen atom passed through the diffusion barrier will

react with Zr cations and form ZrO_2. By measuring the thickness of the stochiometric ZrO_2 layer, the oxygen diffusion flux of the barrier film can be quantified.

The apparatus of the experiment is illustrated in Figure 12. A Zr indicator layer was first deposited on a Si substrate before depositing the metal oxide diffusion barrier, as illustrated in Figure 12a. Then the film stack was oxidized under various conditions to let the oxygen atoms diffuse through the barrier layer. After the oxidation process, any oxygen atoms that reach the Zr surface will react to form ZrO_2, as shown in Figure 12b. The thickness of the ZrO_2 layer and therefore oxygen diffusion flux could be determined by optical characterizations as discussed in Chapter 2.5 and 2.6.

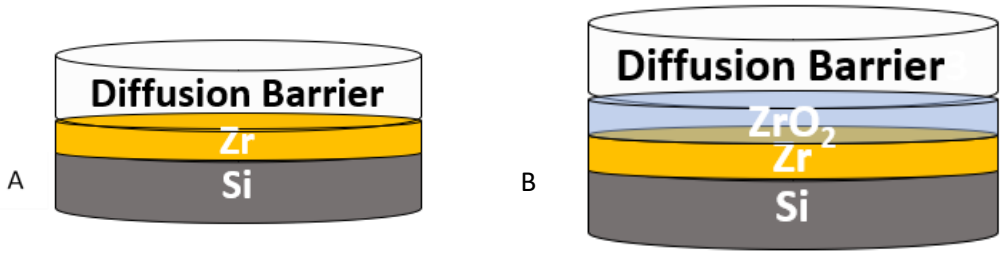

Figure 12. Schematics of quantifying the oxygen diffusion flux using Zr as oxygen indicator layer

- 3.3 Materials Preparation
    - 3.3.1 Film deposition system

Sample stacks were prepared on a one-side polished, 525 µm thick Si substrate. [i]High purity Zr film was prepared by sputter deposition. The base pressure of the deposition system was at or below $2x10^{-6}$ Torr. The Zr target was DC sputtered in an Ar plasma. The gas flow was controlled to be 50 sccm of Ar gas and the pressure during deposition was 5 mTorr. The current supplied to the sputter gun was regulated at 0.5 A resulting in a bias of 293 V. The resulting deposition rate was approximately 80 nm per minute. The Zr indicator layer was deposited for 5 minutes sputters after 1 minute pre-sputter. The resulting film thickness was approximately 400 nm.

The depositions of the Y_2O_3 and Al_2O_3 diffusion barriers were also performed by sputter deposition. Using the off-axis configuration [22], a gradient of film thickness was achieved in a single run. Figure 13 [23] shows the configuration of the substrate and the target, aligned perpendicular to each other. Magnets in the sputter gun confine the plasma over the target. In this arrangement a thicker film is deposited on the substrate side near the target and thinner away from the target. Therefore, a gradient of film thickness was achieved in one run and run-to-run inconsistencies and variations are eliminated.

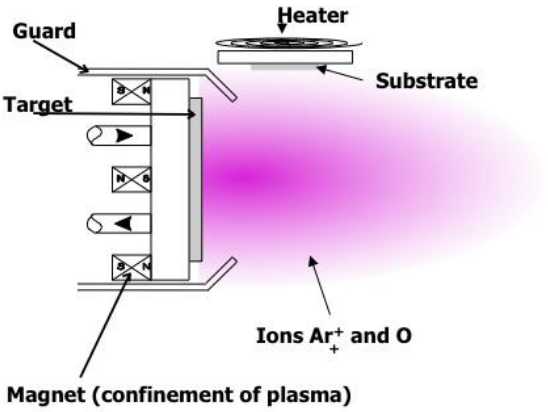

Figure 13. In-chamber view of the off-axis sputtering system

For Y_2O_3 film deposition an RF power of 100 watts was used to sputter high purity Y metal target. The gas flow was a mixture of 15 sccm of Argon and 10 sccm of oxygen to ensure that the film was fully oxidized. The base pressure of the chamber was $2x10^{-6}$ torr and the deposition pressure was 30 mTorr. A test run was performed to characterize the deposition rate profile and the film thickness was measured by profilometry. A liftoff mask comprising a strip of black wax was applied along the center line of the substrate prior to deposition. After film was deposited, the black wax was stripped off by Carbon triachloroethylene, leaving the center line of the substrate uncoated. Film thickness along each

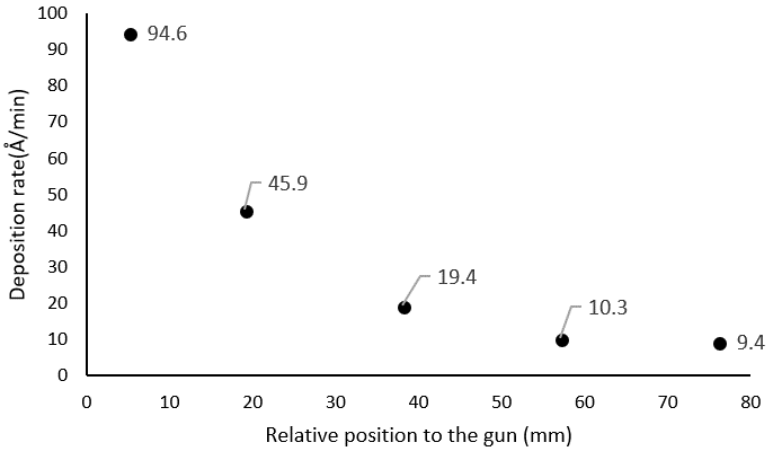

Figure 14. In-chamber view of the off-axis sputtering system

position can be measured using the stylus of a KLA-Tencor P10 profilometer. Figure 14 shows the deposition rate of Y_2O_3 as a function of distance from the sputter gun. The end close to the gun yields a deposition rate of 94.6 Å/min while the far end has a rate of 9.4 Å/mins. Thus, a tenfold thickness gradient can be achieved in a single run. To optimize the sample matrix, test samples were deposited for 5 minutes resulting a Y_2O_3 film thickness of approximately 4.7 nm on thin side and 47.3 nm on thick side.

The Al_2O_3 film was deposition by the same off-axis alignment as the Y_2O_3 samples. For this material the deposition pressure was 30 sccm and the RF power was 100 W. The film thickness and deposition rate were characterized by the same method as Y_2O_3 samples. The deposition rate of the Al_2O_3 film was measured to be 108 Å/min on the thick side and 3 Å/min on the thin side. Two sets of Al_2O_3 samples with different deposition time were prepared. First set of Al_2O_3 samples were sputtered for 14 minutes to obtain a film thickness of approximately 151 nm on the thick side and 4.2 nm on the thin side. Second set of Al_2O_3 samples were prepared to be a lot thinner than the first set of samples. The deposition time for the second set of samples was 210 seconds. The resulting film has 38 nm Al_2O_3 on the thick side and less than 1 nm film on the thin side.

- 3.3.2 Thermal oxidation process

Thermal oxidation of the samples was performed in a tube furnace in atmosphere environment. The air pressure was 760 Torr. With 21% mole fraction of oxygen, the oxygen partial pressure is 160 Torr. Each set of samples was annealed at 300 °C, 400 °C and 500 °C respectively. The effect of repeated heating and cooling was also tested using a second annealing protocol. Thermally cycled samples were annealed 30 mins at the target temperature, cooled down to room temperature, and ZrO_2 thickness was characterized by reflectometry. Then the samples were processed by another run of thermal oxidation at higher temperature, followed by cooling down and thickness

measurement. The process was repeated until samples were fully oxidized. Another set of samples were annealed in a single step at the highest temperature for comparison (i.e., not cycled). The oxidation time of the single-step-anneal samples was equal to the total oxidation time of the thermally cycled samples.

- 3.4 Measurement procedure

After each annealing step optical measurements were taken to infer the thickness of the ZrO_2 layer formed during thermal oxidation. Both a Woollam. spectroscopic ellipsometor and a F50 Filmetrics reflectometer were utilized for optical characterization. Prior to analyzing the testing samples, optical models for the Zr indicator layer, Y_2O_3 and Al_2O_3 layers were constructed using ellipsometry (see Chapter 1.5 for details). For example, a sputtered Y_2O_3 film with known thickness on Si substrate were characterized using the ellipsometor. By building optical model of Δ and Ψ corresponding to the film thickness, the ellipsometor software was able to infer film optical properties, i.e., the refractive index and extinction coefficient as a function of wavelength. Optical models for sputtered Zr and Al_2O_3 film were constructed using the same procedure. After thermal oxidation, a layer of ZrO_2 film formed between the diffusion barrier layer and Zr underlayer. Since the rest of the film stack has known optical properties, the F50 Filmetrics software was able to calculate the unknown ZrO_2 thickness by fitting the reflectance spectrum. In this way the thickness of ZrO_2 layer formed during thermal oxidation was experimentally inferred. The oxygen diffusion flux and permeability of the barrier layer can be calculated using procedure detailed in chapter 1.6.

4. RESULTS

- 4.1 Bare Zr oxidation

To quantify the Zr oxidation with various diffusion barriers, the oxidation characteristics of bare Zr must be characterized and understood. A set of samples were prepared by sputtering a layer of Zr on a Si substrate and annealing the film in the tube furnace. The samples were cooled down at 30 minutes, 60 minutes, 90 minutes and 210 minutes respectively for ZrO_2 thickness measurement. The oxidation curve of sputtered Zr at various temperature is shown in Figure 15.

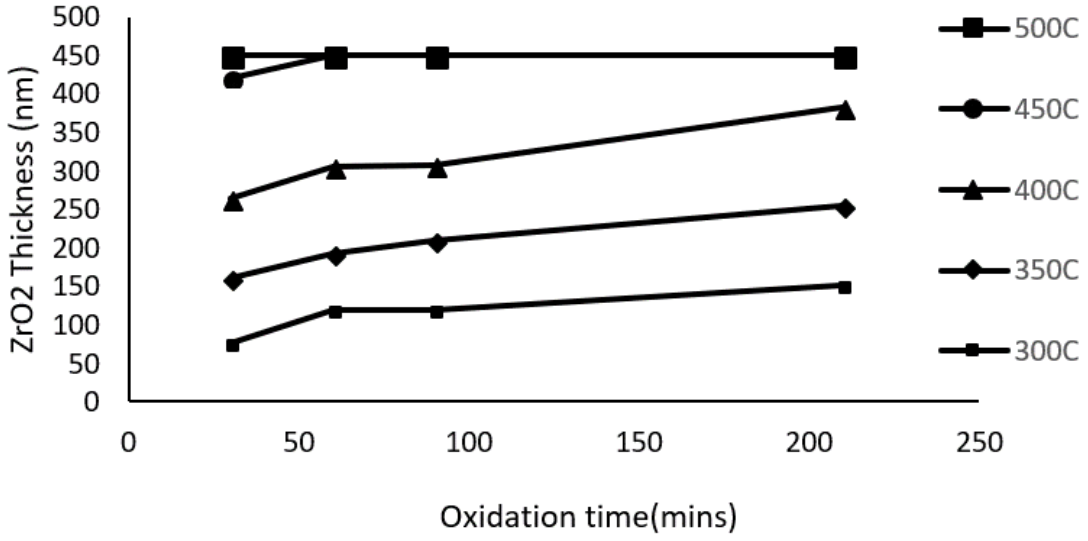

Figure 15. ZrO_2 thickness formation as a function of anneal time under various temperature

The thickness of the bare Zr sample was approximately 400 nm. The greatest ZrO_2 thickness was obtained after the 500 °C and 450 °C anneals and the least amount of ZrO_2 formed after the 300°C anneal. The oxidized film thickness is consistent with full oxidation of the Zr underlayer. The characteristics of the bare Zr oxidation curve agrees with the experimental finding of L. P. H. Jeurgens et al. [5], which was discussed in chapter 1.4. The formation of ZrO_2 due to thermal oxidation can be categorized into two regimes: the fast growth regime and the slow growth regime.

As explained in chapter 1.4, in the fast growth regime, due to the electrostatic potential difference between the zirconium metal and the native zirconium oxide, Zr cations tend to migrate to the oxide-air interface. After a critical oxide thickness is developed, the electric field decreases and can no longer support further Zr cation transport. At elevated temperature, however, the transportation of Zr cations to the interface is made possible by thermionic emission, leading to growth at a slower rate. Figure 15 shows the time dependences for oxide growth, with oxidation speed increasing with increasing temperature. The ZrO_2 growth rates in the slow growth region were different with different temperatures. The oxidation at 400 °C were significantly faster than oxidation at 300 °C and 350 °C. This is consistent with the fact that at 400 °C, thermionic emission is favored compared to emission at lower temperatures, therefore providing quicker Zr transportation to the surface. Similar trends were be seen at 450 °C and 500 °C anneals as samples were all fully oxidized at even the shortest annealing time.

Several procedures were taken to ensure the samples were fully oxidized. Because sputtered samples were likely to show thickness variation across the wafer (the center of the substrate was centered with respect to the target and therefore will develop the greatest thickness compared to the periphery of the substrate). A reference sample was coated by black wax along center line of the Si substrate prior to Zr deposition. After a 5 minutes Zr sputter deposition the black wax was stripped and thickness

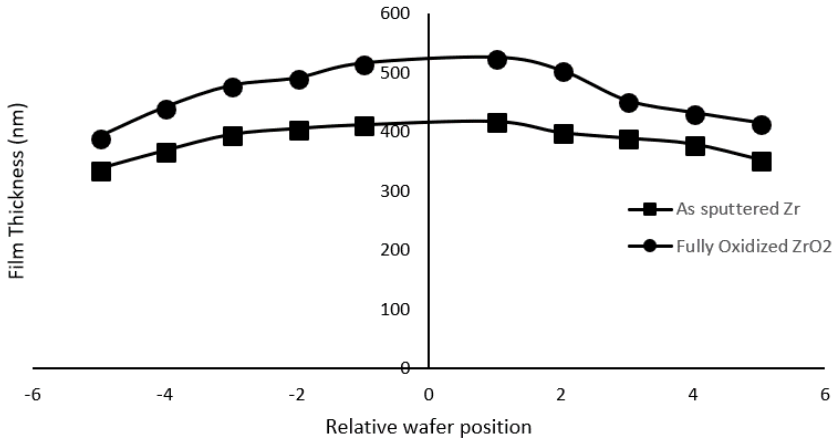

Figure 16. Film Thickness of the as sputtered Zr film and its fully oxidized ZrO_2 film as a function of relative wafer position.

measurements were taken using a KLA-Tencor P10 profilometer. Thickness variation was found between center and edge of the sample, as expected. Figure 16 shows the thickness of the Zr film as a function of position on the wafer. The sample was then annealed at 500 °C for three hours to ensure that it was fully oxidized. The initial Zr film thickness and fully oxidized ZrO_2 thickness are shown in Figure 16. The sputtered Zr film thickness varied from 337 nm to 418 nm between edge and center of the Si substrate. After being fully oxidized, the resulting ZrO_2 film thickness varied from 391 nm to 526 nm.

The effect of thermal cycling on oxidation of bare Zr was also tested. Figure 15 shows that, for oxidation at all temperatures (except the films oxidized at 450 °C and 500 °C, which were, fully oxidized) film growth didn't exhibit a constant rate in the slow growth regime. A second set of Zr samples were annealed under the same conditions except they were annealed 90 minutes nonstop to compare with the current sample. The ZrO_2 thickness comparison of the two sets of samples is shown in Figure 17. Both annealing procedures produced the same thickness at 500 °C, nor surprising as both samples were fully oxidized after the first 30 minute. The samples oxidized at 300 °C and 400 °C for 90 minutes showed a greater ZrO_2 thickness than the equivalent films that were cooled after the 30 minute and 60 minutes steps. At 300 °C, oxidation of Zr under a nonstop 90 minutes anneal yielded a ZrO_2 layer of 97 nm compared with a thickness of 72 nm for the sample then underwent cyclic cooling and heating, a 35% difference in thickness. At 400 °C the ZrO_2 thickness for the nonstop anneal was 296

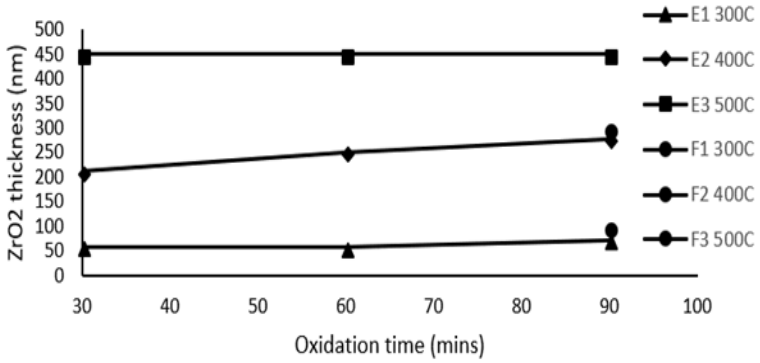

Figure 17. Formed ZrO_2 thickness comparison between different annealing techniques: 90 minutes nonstop vs. cooling down to room temperature every 30 minutes

nm and while the ZrO_2 thickness was 278 nm for the cyclic anneal, i.e., a 6.5% difference in thickness.

To confirm that this unexpected result was not due to potential error in the automated interpretation of reflectance spectrum, the raw reflectance data was analyzed. Figure 18 shows the reflectance spectrum of the oxidized ZrO_2 films obtained under both conditions. The data correspond to the associated data points in Figure 17. Figure 18A shows the film reflectance as a function of incident light wavelength for samples oxidized at 300 °C. The spectrum for the nonstop 90 minutes anneal shows that this sample had the thickest oxide formation, as directly seen by the position of the interference maxima and minima (i.e., they are at longer wavelengths than for the cyclically annealed sample). Based on this method, it can be robustly inferred that the 90 minutes nonstop anneal formed a thicker layer than the film that was cyclically annealed. A similar comparison can be made using the data for 400 °C oxidation as shown in Figure 18B. The data for the film oxidized nonstop for 90 minutes is clearly translated to higher wavelength compared to the

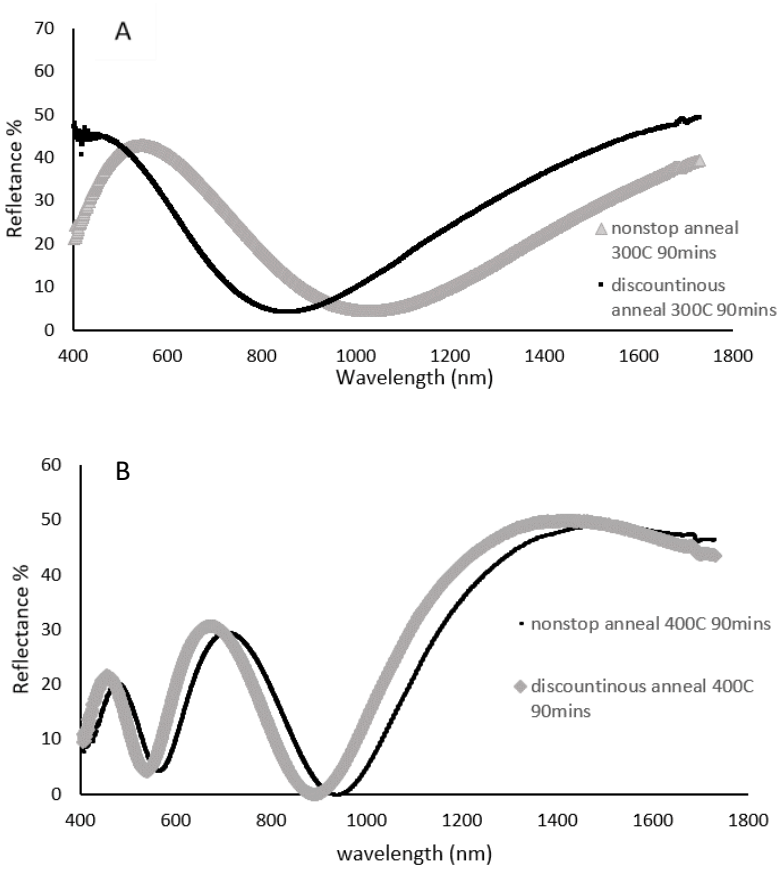

Figure 18. Film reflectance as a function of incident wavelength for oxidized ZrO_2 annealed at A) 300 °C; B)400 °C

data for the cyclic annealed sample, indicating a modest increase in film thickness. Therefore we conclude that at both 300 °C and 400 °C, for the same oxidation time, nonstop annealing yields formation of a thicker ZrO_2 layer than repeating cooling and heating. The mechanism for this difference is unclear but it could be related to the activation of Zr cations transport and the incubation of ZrO_2 film growth, which will be discussed in Chapter 5.

- 4.2 Zr Oxidation with a Y_2O_3 diffusion Barrier

Y_2O_3 diffusion barriers were prepared and tested using the procedure described in Chapter 2.3. Because Y_2O_3 films were sputtered in the off-axis configuration, a thickness gradient was obtained in all Y_2O_3 films. Five spots were marked on the substrate using a sharpie marker. The positions of the spots were approximately at 0 mm, 25 mm, 50 mm, 75 mm and 100 mm along the gradient axis. The thickness of the ZrO_2 film adjacent to the marked spots was measured using reflectometry. As in the case of oxidation of the bare Zr film, the thickness measurement was performed at room temperature after each anneal. Three samples were prepared in order to enable diffusion tests at 300 °C, 400 °C and 500 °C. ZrO_2 thickness as a function of oxidation time at 300 °C s is shown in Figure 19. The thermal oxidation of bare Zr at 300 °C is also shown for comparison with the Y_2O_3 – coated samples. For samples 5 nm of Y_2O_3 the barrier significantly reduced the formation of ZrO_2 from 152 nm to 59 nm for a 300 °C anneal at 210 minutes. The thicker Y_2O_3 diffusion barriers were able to reduce the

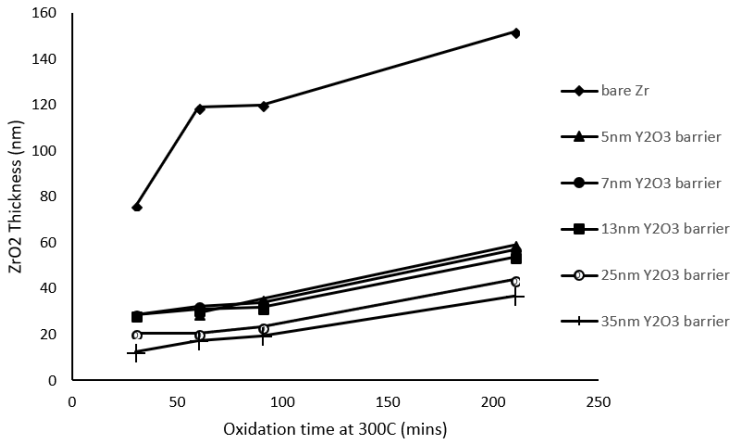

Figure 19. ZrO_2 formation as a function of oxidation temperature for 300 °C anneal.

formation of ZrO_2 even more but failed to entirely block the oxygen diffusion. After 300 °C oxidation for 210 minutes, there was 37 nm of ZrO_2 film formed below the 35 nm Y_2O_3 diffusion barrier.

Similar trends could also be observed in 400 °C and 500 °C oxidation tests. Figure 20 a) and b) show the ZrO_2 thickness formation as a function of oxidation time for 400 °C and 500 °C anneals respectively. Compared to 300 °C oxidation, the effectiveness of a Y_2O_3 film diffusion barrier gradually decreased with increasing temperature. At 400 °C, although the application of 36 nm Y_2O_3 somewhat decrease the ZrO_2 formation from 382 nm to 242 nm, the application of 6 nm of Y_2O_3 failed as oxygen diffusion barrier. As shown in Figure 20 a), after 210 minutes anneal at 400 °C a 382 nm ZrO_2 formed on bare Zr, while 346 nm of ZrO_2 formed on the Y_2O_3 –covered Zr. The 6nm Y_2O_3 barrier failed to block the majority of oxygen atoms from reaching the Zr. It should also be noted that the oxidation rate increased with increasing oxidation time and cooling down cycles. This effect was also magnified by the thickness of the Y_2O_3 barrier. Oxide formation rate increased more on the samples

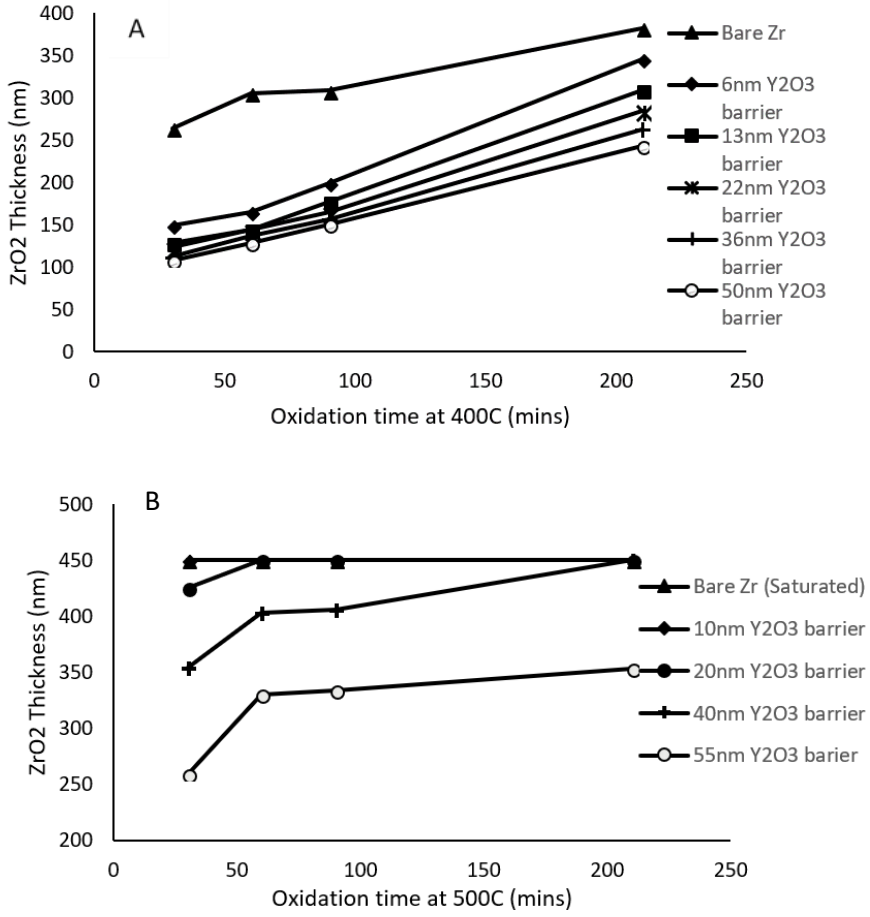

Figure 20. ZrO_2 formation as a function of oxidation temperature for a) 400 °C anneal; b) 500 °C anneal

with thinner Y_2O_3 diffusion barrier. The details will be discussed in Chapter 5. At 500 °C, the Y_2O_3 layer offered even less protection to the Zr film. Samples with 10 nm, 20 nm and 40 nm Y_2O_3 barriers were completely oxidized after a 210 minutes oxidation. The thickest barrier (55 nm) of Y_2O_3 reduced the ZrO_2 formation slightly compared to an unprotected Zr film, to 353 nm. In conclusion, Y_2O_3 was determined to be a poor oxygen diffusion barrier at 300 °C, 400 °C and 500 °C.

The effect of thermal cycling on barrier property of Y_2O_3 was also tested by comparing the ZrO_2 formation of a 90 minutes thermal oxidation under the two different annealing protocols: cooling down to room temperature every 30 minutes vs. nonstop anneal. Measurements were taken for anneals at 300 °C, 400 °C and 500 °C to investigate the temperature dependence. The ZrO_2 formation curve as a function of Y_2O_3 thickness is shown in Figure 21. At 300 °C, the ZrO_2 formation difference between the two annealing protocols was not significant. For both cyclic and non-stop annealed samples, the formation of ZrO_2 decreased with increasing Y_2O_3 thickness, as shown in Figure 21 (a). The repeated cooling sample showed slightly more ZrO_2 formation in the Y_2O_3 thickness ranged from 5 nm to 20 nm than the nonstop annealed sample, but the difference was less than about 4%. Beyond 20 nm of Y_2O_3, the two ZrO_2 formation was independent of protocol, indicating that at 300 °C thermal oxidation, repeated heating and cooling of Y_2O_3 layer had negligible effect on its oxygen diffusion flux.

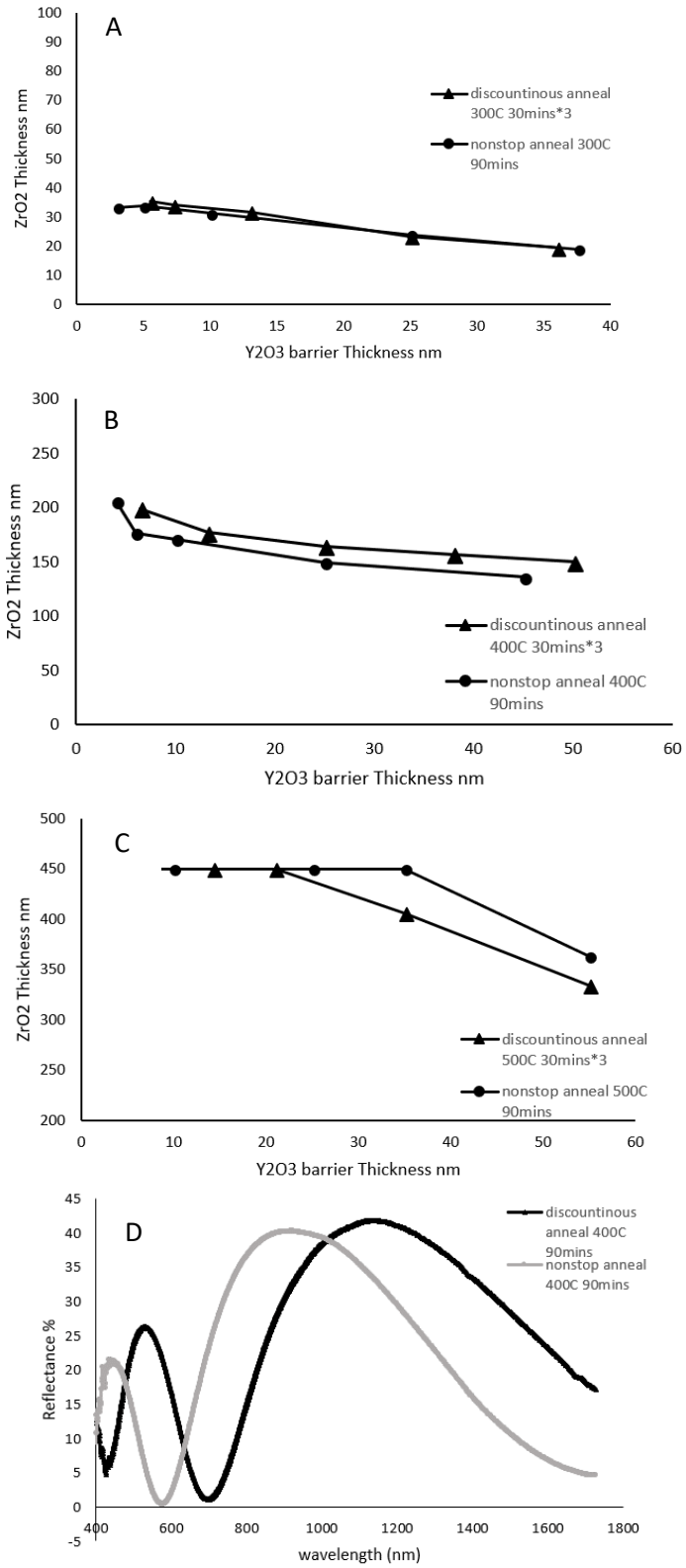

Figure 21. ZrO_2 thickness formation as a function of Y_2O_3 barrier thickness after 90 minutes thermal oxidation at a) 300 °C; b) 400 °C, c)500 °C; d) Reflectance spectrum of samples oxidized at 400 °C for 90mins with 25nms Y_2O_3 diffusion barrier

Figure 21 (b) shows the ZrO_2 thickness formation as a function of Y_2O_3 barrier thickness at 400 °C thermal oxidation. Similar annealing and analyzing procedures had been performed on this set of samples as the 300 °C samples. Similar to the 300 °C oxidized samples, the formation of ZrO_2 decreased with increasing Y_2O_3 thickness for both the discontinuous and non-stop annealed samples. A consistent trend in ZrO_2 thickness difference was observed for all Y_2O_3 layer thickness. The discontinuous-annealed samples formed an average of 15 nm more ZrO_2 compared to the nonstop-annealed samples. The observed result was supported by the films' reflectance spectrum. Figure 21 (d) shows the reflectance spectrum for the two differently annealed samples after 90 minutes oxidation. The two reflectance measurements were taken at the 25 nm Y_2O_3 thickness spots. It can be robustly inferred from Figure 21 (d) that the discontinuous annealed sample had greater optical thickness than the nonstop annealed sample. With the same Y_2O_3 thickness, the discontinuous annealing protocol yielded thicker ZrO_2. Considering that the discontinuous annealed sample had been cooled down from 400 °C to room temperature three times whereas there was only one cooling event for the nonstop annealed sample, it could be concluded that at 400 °C, repeated thermal cycling of Y_2O_3 enhanced oxygen diffusion through the film.

The same procedures were followed for 500 °C oxidation; the ZrO_2 thickness as a function of Y_2O_3 thickness is shown in Figure 21 (c). At 500 °C, most of the samples were fully oxidized after the 90 minutes oxidation for both annealing protocols. It was also observed that thicker Y_2O_3 barrier yielded less ZrO_2 formation. However, unlike the 400 °C oxidation, the nonstop annealing procedure at 500 °C resulted in a thicker ZrO_2 layer compared to the cyclic protocol. The mechanism for this trend is unclear but a hypothesis will be discussed in Chapter 5.

- 4.3 Zr oxidation with Al_2O_3 diffusion barrier

Al_2O_3 diffusion barriers were deposited on top of Zr for 14 minutes to obtain a film thickness of approximately 151 nm on the thick side and 4.2 nm on the thin side, as described in Chapter 2.3.1. Then the samples were annealed and tested for ZrO_2 thickness every 30 minutes of oxidation following the same procedure as the Y_2O_3 samples. Three samples were prepared and oxidized at 300 °C, 400 °C and 500 °C respectively. Five spots were marked on each sample using a sharpie marker. The positions of the spots were approximately at 0 mm, 25 mm, 50 mm, 75 mm and 100 mm along the gradient axis. At the end of each cool down optical reflectometry measurements were taken at each marked spot. The ZrO_2 thickness formation as a function of oxidation time with a range of Al_2O_3 barrier thickness is shown in Table 1.

Table 1. Measured ZrO_2 thickness as a function of oxidation time and Al_2O_3 barrier thickness for 300 °C, 400 °C and 500 °C oxidation.

Al2O3 thickness (nm)	ZrO2 thickness (nm)								
	300°C Oxidation time(min)			400° C Oxidation time(min)			500°C Oxidation time(min)		
	30	60	180	30	60	180	30	60	180
151	0	0	0	0	0	0	0	0	0
52	0	0	0	0	0	0	0	0	0
20	0	0	0	0	0	0	0	0	0
12	0	0	0	0	0	0	0	0	0
5	0	0	0	0	0	0	0	0	0

Table 1 indicates that no ZrO_2 formed in any of the oxidation experiments. Even at 500 °C oxidation, an Al_2O_3 layer of 5 nm blocked all oxygen reaching Zr layer surface.

To investigate the Al_2O_3 film barrier property as a function of film thickness, an ultrathin Al_2O_3 film was deposited on Zr indicator layer using off-axis sputter deposition. The deposition time for the second set of samples was 210 seconds. The resulting film had 38 nm Al_2O_3 on the thick side and

less than 1 nm film on the thin side, as described in Chapter 2.3.1. Three samples were thermally oxidized at 300 °C, 400 °C and 500 °C respectively following the procedure in Chapter 2.3.2 for 30 minutes. At the end of thermal oxidation, after samples had been cooled down to room temperature, ZrO_2 thickness were measured from the thickest Al_2O_3 to the thinnest Al_2O_3. Measured ZrO_2 thickness as a function of Al_2O_3 barrier thickness is shown in Figure 22.

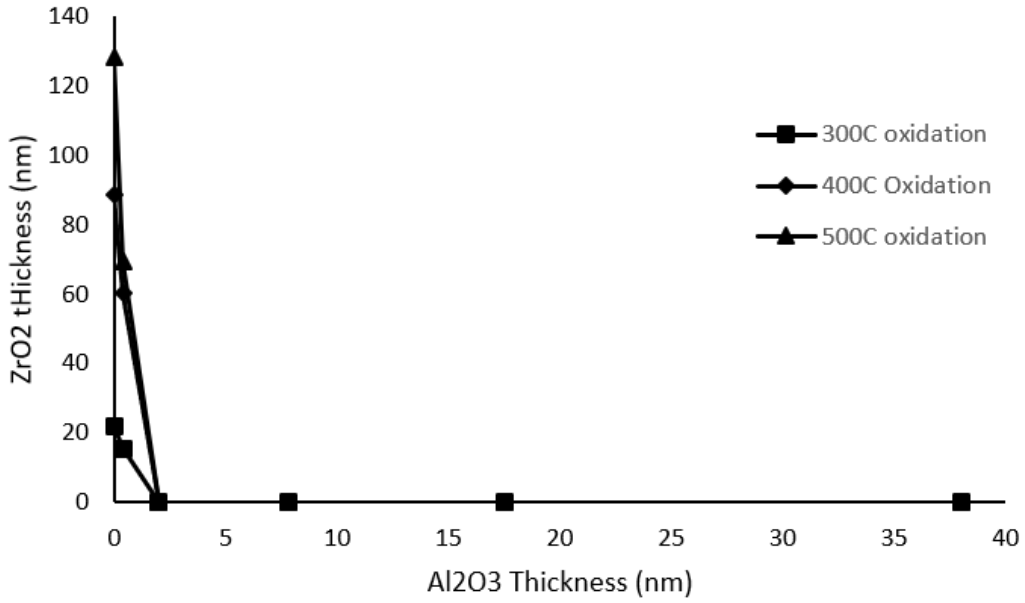

Figure 22. ZrO_2 thickness as a function of Al_2O_3 diffusion barrier after 30 minutes anneal at 300 °C, 400 °C and 500 °C.

Figure 22 showed that an Al_2O_3 diffusion barrier of 2 nm or greater was sufficient to block all oxygen diffusion at any temperature up to 500 °C. However, for all three oxidation temperatures, ZrO_2 formation was detected when Al_2O_3 thickness was below 1nm, and the thickness of the formed ZrO_2 layer increased with increasing oxidation temperature. An increase in ZrO_2 layer thickness (69 nm to 129 nm) was observed for 500 °C oxidation when the Al_2O_3 thickness decreased from an estimated 0.8 nm to an estimated 0.2 nm (the Al_2O_3 thickness was estimated using a scaled deposition rate profile because it was no longer directly measurable using ellipsometry or reflectometry). It is unclear whether the Al_2O_3 layer comprised a continuous film at 0.2 nm average

thickness; nevertheless, the ZrO_2 layer formation was still significantly inhibited by the Al_2O_3 layer. We conclude that at up to 500°C the oxygen permeability is negligibly small for complete coverage of Al_2O_3.

5. DISCUSSION

- 5.1 Calculation of the oxygen atoms diffusion flux

As derived in Chapter 1.6.2, oxygen permeability of a diffusion barrier can be related to the oxygen diffusion flux, *J*, across the film, the thickness of the diffusion barrier film, *t*, the solubility of oxygen atoms in the diffusion barrier, *S*, and the concentration of oxygen in air, C_1. The relationship is given by:

$$P = \frac{J * t * S}{C_1}$$

Atmospheric air contains 21% by volume of oxygen. One liter of air contains 210 mL of oxygen. According to the ideal gas law, under standard condition, the volume of 1 mole of gas is 22.4 Liters. So 210 mL of oxygen contains 0.0094 mole O_2 molecules, or 0.0188 mole oxygen atoms. Therefore, the numerical value of C_1 is 0.0188 mole/cm^3. For fully oxidized Y_2O_3 and Al_2O_3 films, the solubility of oxygen atoms is approximated to be the oxygen concentration in the compound. The oxygen atoms solubility was determined to be 0.0666 mole/cm^3 for Y_2O_3 and 0.116 mole/cm^3 for Al_2O_3.

The atomic diffusion flux *J* can be experimentally determined by calculating the number of oxygen atoms that have diffused through the film per unit area and unit time. The number of oxygen atoms passing through the diffusion barrier is equal to the number of oxygen atoms that react to form ZrO_2, which can be determined quantitatively from the thickness of the formed ZrO_2

layer, *t*. The molar density of oxygen atoms in fully oxidized ZrO_2 is 0.092 mol/cm^3. Therefore, the oxygen atoms diffusion flux can be estimated by:

$$J = \frac{t * 0.092}{time} \frac{mole}{cm^2 * sec}$$

With experimentally determined ZrO_2 thicknesses, the oxygen diffusion flux and permeability can be easily calculated. Figure 23 showed the oxygen diffusion flux as a function of Y_2O_3 barrier thickness after 30 minutes, 60 minutes, 90 minutes oxidation respectively.

It can be concluded from Figure 23 that oxygen atoms diffuse through Y_2O_3 at a faster rate at higher temperatures; the flux at 500 °C was more than twice of that at 400 °C. The relationship of flux and Y_2O_3 barrier thickness for lower temperature oxidation (300 °C and 400 °C) was quite different from that for higher temperature oxidation (500 °C). At 300 °C and 400 °C oxidation, the oxygen atoms diffusion flux had little dependence on Y_2O_3 barrier thickness. The rate of oxygen diffusion remained approximately constant, independent of the thickness of the Y_2O_3 diffusion barrier. At 500 °C flux showed strong dependence on Y_2O_3 thickness. Overall the oxygen diffusion flux at 500 °C showed negative correlation with Y_2O_3 barrier thickness although with a discrepant value for approximately 25 nm Y_2O_3 barrier thickness.

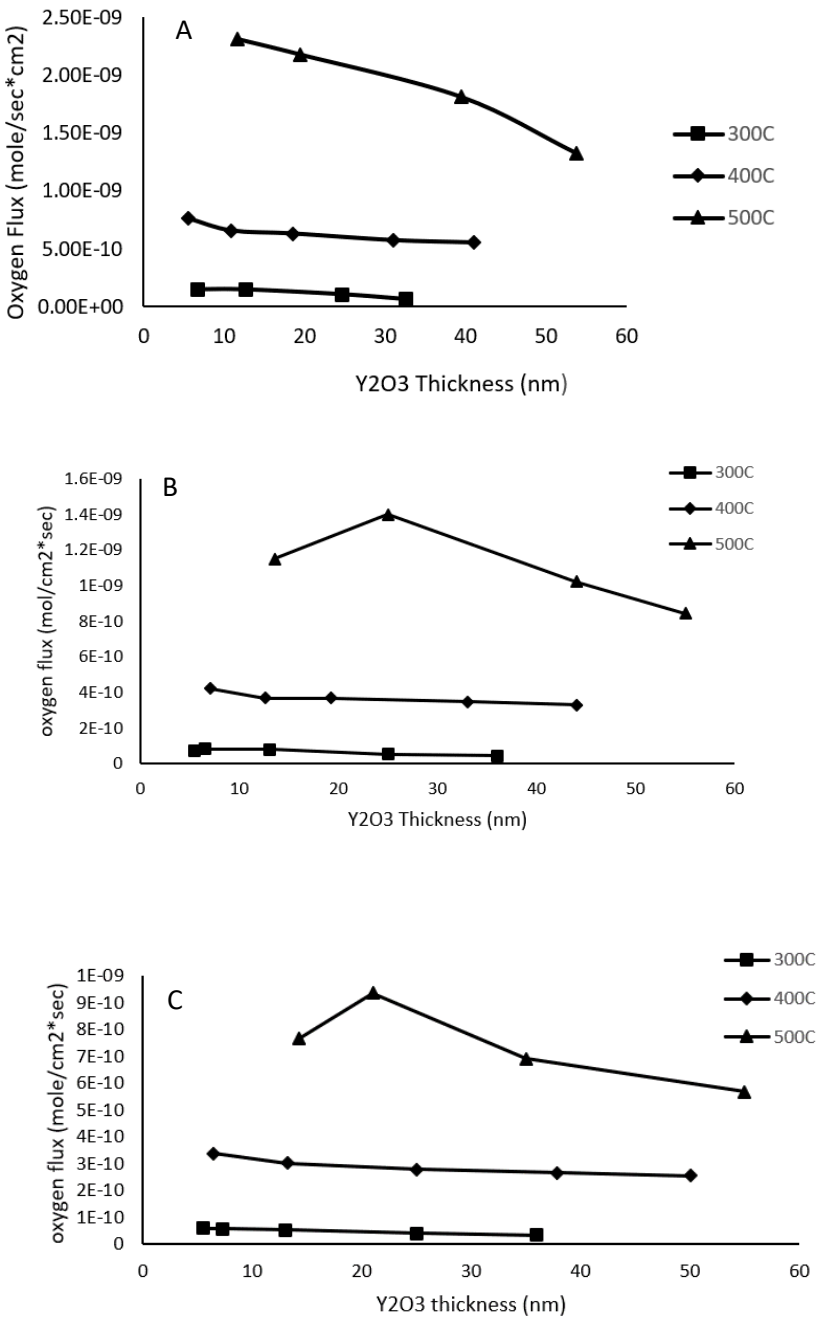

Figure 23. Oxygen atoms diffusion flux as a function of Y_2O_3 film thickness oxidized after A. 30 minutes; B. 60 minutes; C. 90 minutes.

From the definition of diffusion flux, $J=-D\,\partial C/\partial x$, the flux J should be inversely correlated to barrier thickness, assuming that the diffusivity D is constant within the barrier. The constant value for the flux at 300 °C and 400 °C indicates that the oxygen diffusion had small dependency on bulk diffusion controlled by Fick's law as described in Chapter 1. Instead another mechanism that dominates oxygen diffusion must be invoked. One possible explanation could be the existence of micro-pipes that thread the Y_2O_3 barrier. Micro-pipes would provide a rapid path for oxygen atoms to travel from the top surface to the bottom surface of the Y_2O_3, leading to a diffusion flux that is independent of film thickness. The total flux would be a sum of bulk diffusion and pipe-related diffusion. We speculate that the bulk oxygen diffusion flux in Y_2O_3 increases rapidly with increasing temperature, so that at 500 °C the oxygen diffusion rate due to the bulk mechanism dominates over the pipe-related diffusion, leading to behavior that is more consistent with Fick's Law. Future studies are required to identify the sources and types of the pipes.

- 5.2 Oxygen permeability calculation and dependence

Using equation 4 as discussed in Chapter 1.6.2, the oxygen permeability can be easily calculated given the measured diffusion flux and thickness of the barrier film. The Y_2O_3 film oxygen permeability is plotted as a function of Y_2O_3 thickness in Figure 24. This figure shows that Y_2O_3 film permeability increases with oxidation temperature as expected. As discussed in chapter 1.6.2, film oxygen permeability is proportional to the product of oxygen diffusion flux and barrier thickness. In Chapter 4.1, we had concluded that at 300 °C and 400 °C oxidations, oxygen diffusion flux remained unaffected by the Y_2O_3 film thickness. Therefore, with increasing Y_2O_3 thickness, the apparent oxygen permeability increases, as illustrated in Figure 24. A possible explanation was presented in Chapter 4.1.

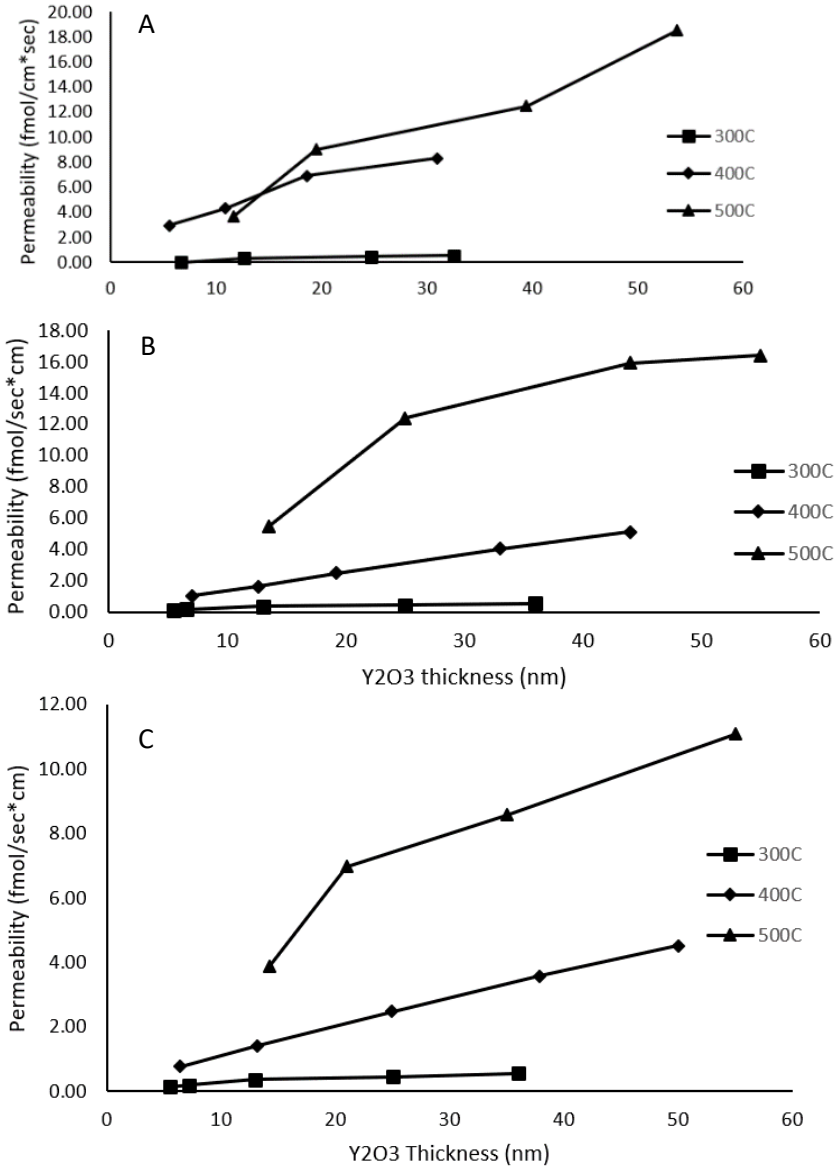

Figure 24. Oxygen permeability as a function of Y_2O_3 film thickness oxidized after A. 30 minutes; B. 60 minutes; C. 90 minutes.

Complete coverage alumina films with thickness greater than 2 nm had zero oxygen diffusion flux when oxidized at 300 °C, 400 °C and 500 °C environment. Therefore, the oxygen permeability of alumina film was experimentally determined to be negligible.

- 5.3 Effect of thermal cycling on barrier properties

Repeated heating and cooling of thin film materials often has deleterious effects on thin film properties. Frequent thermal expansion and contraction of the thin films often creates defects that are expected to enhance diffusion. The effect of thermal cycling on Y_2O_3 and Al_2O_3 thin films was studied by the cycling tests detailed in Chapter 3.2. The ZrO_2 layer formation curve with and without the barrier was shown in Figure 19 and 20, with their diffusion behavior discussed in Chapter 3.2. Here only the effect of thermal cycling will be discussed.

Referring to Figures 17, 19 and 20, several observations can be made regarding ZrO_2 formation during each anneal and cool down. Figure 17 indicates that for bare Zr oxidation, a thicker ZrO_2 layer formed if the Zr was continuously oxidized for 90 minutes than when it was cooled down to room temperature every 30 minutes. This behavior was also observed in oxidation with involving the Y_2O_3 diffusion barrier (Figure 19 and 20). The bare Zr oxidation curve has a dramatic increase in the ZrO_2 formation rate from 90 minutes to 210 minutes when the samples were annealed for 120 minutes without cool down for experiments at all temperature (300 °C, 400 °C and 500 °C). Therefore, it can be concluded that repeated temperature cycling decreased the ZrO_2 formation from compared to bare Zr oxidation. A possible reason could be due to the thermal activation of the oxidation process. Based on the double current model introduced in Chapter 1.4, for Zr to form ZrO_2, Zr cations must transport to the surface of the Zr layer compensated by the transporting of electrons. It was observed that the repeated heating and cooling reduced the formation of ZrO_2 when Zr cations outward diffusion was the limiting step of the oxidation process. Therefore, it could be indicated that repeated heating and cooling reduced the efficiency of ZrO_2 formation by reducing the efficiency of Zr cations diffusion. Because there is an activation energy associated with Zr cations diffusion, more thermal cycles require more energy to overcome this energy barrier, thus reduce the ZrO_2 formation.

Figure 19 and Figure 20 indicate that the Y_2O_3 diffusion barrier behaves differently with regard to growth of the ZrO_2 layer as a function of thermal cycles compared to the uncoated Zr. With a Y_2O_3 barrier at 400 °C, a significantly thicker ZrO_2 layer formed after the thermal cycling protocol whereas at 500 °C, a thicker ZrO_2 layer formed on the non-stop annealed samples--behaving more like bare Zr oxidation. The increase in ZrO_2 formation at 400 °C could be explained by enhanced oxygen diffusion. The Y_2O_3 was reported to have a thermal expansion coefficient of $8.1x10^{-6}$ K^{-1} whereas the Si substrate has only $2.6x10^{-6}$ K^{-1}. During repeated heating and cooling, the stress induced by thermal expansion and contraction of the Y_2O_3 layer could induce stress-related defects such as cracks in the growing ZrO_2 layer. As a result, the diffusion of oxygen could be enhanced. At 500 °C, oxygen diffusion was enhanced the same way, but ZrO_2 formation was limited by Zr cations diffusion. At 500 °C, the Y_2O_3 layer was nearly transparent to oxygen and the oxidation behavior was nearly identical to bare Zr oxidation. Therefore, although there was adequate supply of oxygen anions, Zr oxidation was limited by Zr cations transportation. The enhanced oxygen diffusion in Y_2O_3 film didn't contribute to ZrO_2 formation because the process lacked Zr cations. It could be inferred that when the oxidation process is limited by oxygen diffusion, thermal cycles of Y_2O_3 diffusion barrier would increase the ZrO_2 formation by increasing the oxygen diffusion rate; when vice versa, thermal cycles of Y_2O_3 diffusion barrier would reduce the ZrO_2 formation by reduce the Zr cations transport.

- 5.4 Source of errors

Experimental and systematic errors reduce the accuracy of the result. Therefore it is important to understand the source of errors and how they could impact the result.

- 5.4.1 Errors from Zr optical model

Major uncertainty arose from relating the sample reflectance spectrum to the thickness of the ZrO_2 film. The reflectance spectrum provides information about the thickness of the film if optical properties are known such as reflective index and extinction coefficient. It is easy to compare optical thickness of two films by counting the reflective interferences of each spectrum. However, accurate measurement of each film thickness in a film stack requires exact optical model to be built in Filmetrics system. As mentioned in Chapter 1.5, Al_2O_3, Y_2O_3 and ZrO_2 are optically transparent with low extinction coefficient, therefore provide high accuracy in the reflectance spectrum. On the other hand, optical model for the Zr layer were built based on a sputtered Zr sample. Zr as a metal has low refractions therefore systematic error could occur when analyzing a light spectrum refracted from Zr surface. This error came with the nature of the Zr film and could be accounted as systematic error. It existed in all tested samples and could affect the measured thickness of the ZrO_2 layer but should not change the trends observed in Chapter 4.

- 5.4.1 Experimental errors

Systematic and random errors could occur due to uncertainty in experimental setup. Sources of experimental error could come from difference in experimental environment and procedure. For example, the thermal cycling process requires the quenching rate to be constant for all runs, however, due to the uncertainty of air flow rate, the quenching rate might differ slightly, result in slight difference in diffusion barrier contraction. Moreover, ZrO_2 thickness measurements were required to be taken at the exact location each time they finished a thermal cycle. A slight difference in measurement location could produce misrepresentative date. These types of errors are generally avoidable and were minimized by pre-marking the testing spots and by careful and precise alignment with the marks.

6. SUGGESTIONS FOR FUTURE RESEARCH

Oxygen diffusion mechanism in Y_2O_3 thin film involving bulk diffusion and pipe diffusion was proposed after analyzing its oxygen diffusion behavior. Future experiments, such as cross section TEM, are required to confirm the existence of micro-pipes.

7. CONCLUSION

This work has investigated the oxygen permeability of Y_2O_3 and Al_2O_3 thin films as a function of oxidation temperature, film thickness and thermal cycles. Sputtered Y_2O_3 and Al_2O_3 were deposited on Zr for oxidation tests. Amorphous Y_2O_3 was determined to be a poor diffusion barrier against oxygen. Its oxygen permeability ranged from $1.40x10^{-12}$ to $2.32x10^{-9}$ $molcm^{-1}sec^{-1}$ with different oxidation temperature, time and barrier thickness. The oxidation and oxygen diffusion behavior at 500°C were significantly different than the 300 °C and 400 °C oxidations. It was experimentally determined that the oxygen diffusion flux in Y_2O_3 had little dependence on Y_2O_3 barrier thickness below 400 °C and that the flux decreases with increasing Y_2O_3 thickness at 500 °C. We propose a possible diffusion mechanism involving bulk diffusion and pipe diffusion. Further experiments are needed to confirm this. Experiments also show that the Y_2O_3 diffusion barrier reacts differently to cycled heating/cooling as compared to a single heating event. We conclude that Y_2O_3 does not form a reliable oxygen diffusion barrier. Amorphous Alumina films were tested using the same procedure as the Y_2O_3 films. Complete coverage alumina film with thickness greater than 2 nm exhibited negligible oxygen diffusion flux and permeability at 300 °C, 400 °C and 500 °C. Alumina thin film are very effective as oxygen diffusion barriers, up to at least 500°C in air.

REFERENCES

[1] H. Kim, C. Detavenier, O. Van Der Straten, S. M. Rossnagel, A. J. Kellock, and D. Park, "Robust diffusion barrier for Cu-interconnect technology with subnanometer thickness by metal-organic plasma-enhanced atomic layer deposition," *J. Appl. Phys.*, vol. 14308, no. 2005, p. 98, 2007.

[2] A. Ibidunni, A. J. Davenport, and H. S. Isaacs, "Characterization of the Oxidation of Tantalum," *Surf. Interface Anal.*, vol. 20, no. November 1991, pp. 559–564, 1993.

[3] S. W. Jones, "Diffusion in Silicon."

[4] J. Crank, "THE MATHEMATICS OF DIFFUSION," pp. 2–11, 1975.

[5] A. H. Heuer, "Oxygen and aluminum diffusion in α-Al2O3: How much do we really understand?," *J. Eur. Ceram. Soc.*, vol. 28, no. 7, pp. 1495–1507, 2008.

[6] Y. Oishi and W. D. Kingery, "Self-Diffusion of Oxygen in Single Crystal and Polycrystalline Aluminum Oxide," *J. Chem. Phys.*, vol. 480, no. 1960, p. 33, 2006.

[7] L. P. H. Jeurgens, A. Lyapin, and E. J. Mittemeijer, "The mechanism of low-temperature oxidation of zirconium," *Acta Mater.*, vol. 53, no. 18, pp. 4871–4879, 2005.

[8] G. Bakradze, "Initial oxidation of zirconium: oxide-film growth kinetics and mechanisms," 2011.

[9] T. S. Fdms, A. Piegari, E. Masetti, and L. F. Sottlh, "Thin film thickness measurement: A comparison of various techniques," *Thin Solid Films*, vol. 124, pp. 249–257, 1985.

[10] S. S. Chauhan, "Ellipsometry for measuring the thickness of thin films," 2010.

[11] H. Fujiwara, "Spectroscopic Ellipsometry: Principles and Applications," *Spectrosc. Ellipsom. Princ. Appl.*, vol. 57, no. 7, p. 82, 2007.

[12] A. M. Duclos, J. Y., Taptue, *Polarization*, vol. 2. 2015.

[13] I. Woollam Co., "A short course in Ellipsometry." .

[14] "Operation Manual for the FilMetrics F50." p. 35, 2013.

[15] B. Wozniak and J. Dera, *Light Absorption in Sea Water*. .

[16] B. R. M. Felder and G. S. Huvard, *PERMEATION , DIFFUSION , AND SORPTION OF GASES AND VAPORS*, vol. 16. 1980.

[17] E. L. Courtright, J. T. Prater, C. H. Henager, and E. N. Greenwell, "Oxygen permeabiliy for selected ceramcix oxides in the range 1200C to 1700C," 1991.

[18] R. Nakamura *et al.*, "Diffusion of oxygen in amorphous Al_2O_3, Ta_2O_5, and Nb_2O_5," *J. Appl. Phys.*, vol. 116, no. 3, p. 33504, 2014.

[19] P. Auerkari, "Mechanical and physical properties of engineering alumina ceramics," 1996.

[20] H. Watanabe, N. Yamada, and M. Okaji, "Linear Thermal Expansion Coefficient of Silicon from 293 to 1000 K," *Int. J. Thermophys.*, vol. 25, no. 1, p. 227, 2004.

[21] J. Kitamura, H. Mizuno, N. Kato, and I. Aoki, "Plasma-Erosion Properties of Ceramic Coating Prepared by Plasma Spraying," *Mater. Trans.*, vol. 47, no. 7, p. 7, 2006.

[22] R. B. Van Dover and L. F. Schneemeyer, “The Codeposited Composition Spread Approach to High-Throughput Discovery / Exploration of Inorganic Materials,” *Macromol. Rapid Commun.*, vol. 25, pp. 150–157, 2004.

[23] Steven Daniel Kirby, “Electrionic and optical properties of oxide thin films,” 2009.

[i] Several attempts have been made to deposit the Zr indicator layer on the Si substrate. First set of samples were coated with e-beam evaporated Zr. Zr has a relatively high melting temperature (1855°C) so at the operating temperature of the e-gun, the chamber was also heated up significantly and started to out gas. Zr films deposited by such method had large amount of oxygen atoms incorporated in the film and the optical properties changed accordingly. Therefore, the e-gun evaporated Zr film could not be used for optical analysis.